

1 Analysis of Neptunium Oxides Produced Through Modified Direct 2 Denitration

3 Kathryn M. Peruski^{1*}, Connor J. Parker¹, Samantha K. Cary¹

4
5 ¹ Oak Ridge National Laboratory, 1 Bethel Valley Road, Oak Ridge, TN, 37830

6
7 *Corresponding author: Kathryn M. Peruski, Oak Ridge National Laboratory, 1 Bethel Valley Road, Oak Ridge,
8 TN, 37830, USA, Phone: 865-341-0658, E-mail: peruskikm@ornl.gov

9
10 **Keywords:** Neptunium dioxide, electron microscopy, X-ray diffraction, modified direct denitration, radioisotope
11 thermoelectric generator

12 Abstract

13
14 Production of neptunium-237 (²³⁷Np) target materials for plutonium-238 (²³⁸Pu) radioisotope
15 thermoelectric generators (RTGs) for deep space exploration requires advanced chemistry and
16 engineering development. Currently, the domestic Pu-238 Supply Program at Oak Ridge National
17 Laboratory produces neptunium dioxide (NpO₂) for target material using a modified direct denitration
18 (MDD) flowsheet. Although the chemistry, reaction mechanisms, and product characteristics of MDD are
19 well understood for uranium, corresponding studies of the neptunium system are still needed to continue
20 optimization of target material properties, production equipment design, and production flowsheets. The
21 objective of this work is to characterize crystalline phases, morphology, surface texture, and particle size
22 of NpO₂ produced via MDD reactions. Solid-phase characterization techniques, including powder X-ray
23 diffraction (pXRD) and scanning electron microscopy with energy-dispersive spectroscopy
24 (SEM-EDS), were employed to achieve this objective. Subsequent data processing using the
25 Morphological Analysis for Material Attribution (MAMA) software was performed to analyze particle
26 morphology and size. Broadly, the powders were found to contain a mixture of NpO₂ and Np₂O₅ after
27 denitration with a variety of morphologies. After high-firing, the product was found to be NpO₂ with a
28 typical polycrystalline oxide morphology and a grain size ranging from 0.72 to 0.94 μm. These analyses
29 provide knowledge on the reaction pathway for a non-traditional NpO₂ synthesis method and offer
30 additional unique insight into production-scale environments for transuranic materials.

31 32 1. Introduction

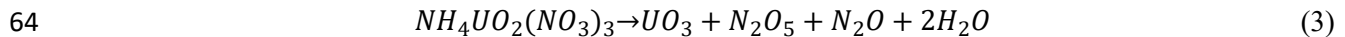
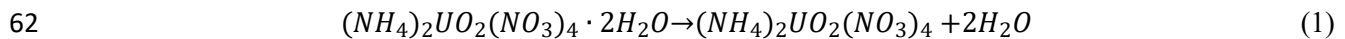
33 Radioisotope thermoelectric generators (RTGs) utilize the decay heat of the radioisotope
34 plutonium-238 (²³⁸Pu) to produce power for deep space exploration applications. This specialized source
35 of thermal power is crucial for ongoing NASA mission requirements, which has production goals of
36 1.5 kg/year on average of high-assay heat source plutonium oxide (HS-PuO₂) by the year 2026. The focus
37 on power systems utilizing ²³⁸Pu was reignited in the early 2000s upon assessment of available sources
38 and NASA's projections of its use in future missions. The reestablishment of the domestic supply of ²³⁸Pu
39 was driven by evaluations of domestic and foreign sources, which identified that NASA's mission
40 requirements outpaced the domestic stockpile and recognized the unfavorable nature of foreign
41 procurement of ²³⁸Pu due to national security concerns.¹

42 To produce ²³⁸Pu, neptunium-237 (²³⁷Np) target material is irradiated and undergoes neutron
43 capture.² This production method for ²³⁸Pu is well established, dating back to the 1960s.³ The domestic
44 ²³⁸Pu production program involves key efforts around the DOE complex: ²³⁷Np targets are produced at

45 Oak Ridge National Laboratory (ORNL) and subsequently irradiated at the High Flux Isotope Reactor
46 (HFIR) at ORNL and the Advanced Test Reactor (ATR) at Idaho National Laboratory (INL).¹ The current
47 flowsheet for production employs neptunium dioxide (²³⁷NpO₂) powder, which is blended with aluminum
48 (Al) metal powder into a cermet pellet to improve thermal conductivity during irradiation. The current
49 composition of ²³⁷NpO₂/Al pellets is 20% vol. ²³⁷NpO₂, 70% vol. Al, and 10% vol. void space.⁴ Following
50 target fabrication and irradiation, targets undergo post-irradiation processing for ²³⁸Pu purification and
51 ²³⁷Np recycling.^{5, 6}

52 The domestic ²³⁸Pu supply program at ORNL fabricates ²³⁷NpO₂ target material through the
53 Modified Direct Denitration (MDD) process. The MDD produced ²³⁷NpO₂ is the reference target material
54 for all US ²³⁸Pu production for RTGs. The MDD flowsheet synthesizes oxide materials from starting
55 nitrate solutions using a rotary kiln designed to produce free-flowing powders.⁷ This process and
56 associated engineering design were developed in the 1980s as part of flowsheets for uranium (U) or
57 mixed-oxide (MOX) fuel production.⁸⁻¹⁰ This system is termed *modified* because instead of starting with a
58 pure uranyl nitrate solution, the uranyl nitrate-ammonium nitrate double salt is denitrated. Double salt is
59 employed to improve fuel pellet ceramic properties.¹⁰ The generalized reaction mechanism for the
60 decomposition of the uranium double salt to UO₃ is described by Notz and Haas:¹⁰

61



65

66 The first dehydration step (Eq. 1) occurs around 40°C, then loss of NH₄NO₃ at 170°C occurs, and the final
67 conversion step (Eq. 3) begins at 270°C.¹⁰ It is important to note that this series of reactions produces
68 UO₃, which must be subsequently converted to UO₂. The generalized reaction mechanism was more
69 recently confirmed by Kim et al.¹¹ Given the recognized need for ²³⁷NpO₂ for targets in the ²³⁸Pu
70 production flowsheet, the MDD process was adapted for ²³⁷NpO₂ production.^{4, 5, 12, 13} ORNL has been
71 testing and employing this flowsheet for ²³⁷NpO₂ target development for over a decade; however,
72 continual optimization of ²³⁷NpO₂ target material and fabrication methods is paramount for meeting
73 ongoing space power system needs.

74 Despite the proven application of this flowsheet, thorough evaluation of the Np-specific
75 chemistry is needed. The initial flowsheet development and process chemistry research on modified
76 denitration reactions focused on U chemistry. Although U and Np have some chemical similarities given
77 that they are both actinide elements, important differences exist in their aqueous chemistry. Uranium is
78 most stable as UO₂²⁺, whereas Np is most stable as NpO₂⁺ or Np⁴⁺.¹⁴ In practice, the U flowsheet is based
79 on initial U oxidation state of (VI), whereas the Np flowsheet employed at ORNL adjusts the Np
80 oxidation state to (V).⁶ These differences in oxidation state and solution chemistry within the actinide
81 series may affect the synthesis and reaction mechanisms toward oxide production.

82 While MDD has become the standard in the ²³⁸Pu flowsheet, most production-scale NpO₂
83 chemical flowsheets utilize a batch oxalate precipitation and calcination method, which originated in the
84 1960s, including what was used at Savannah River Site's HB-line.^{3, 15-18} The synthesis of NpO₂ via
85 oxalate precipitation and calcination is a well-established chemical system. Significant research has been
86 performed on production-scale material, including study of the physical and chemical properties of the

87 HB-line material.^{15, 16, 19} Additionally, reaction mechanisms on the decomposition of Np(IV) oxalate are
88 reported.^{20, 21}

89 Although the reaction mechanisms and material properties of the Np oxalate-oxide system and of
90 the U modified denitration system have been elucidated, the community still lacks information on Np
91 modified denitration reactions and oxide produced through this pathway. The objective of this work is to
92 characterize crystalline phases, morphology, surface texture, and particle size of NpO₂ produced via
93 modified denitration reactions. Tracking and comparing the physical and chemical characteristics of the
94 MDD product is crucial for identification of any variability in the production process and optimization of
95 production. Beyond qualitative description of the oxides, special attention was given to quantitative
96 analysis of particle size and morphology of the materials studied using Morphological Analysis for
97 Material Attribution (MAMA). The MAMA software has been applied for quantitative analysis of
98 uranium oxide morphology^{22, 23}; however, application of this software to Np is lacking in the open
99 literature. There are additional challenges to handling transuranic materials such as ²³⁷Np, which often
100 preclude the characterization techniques that seem routine for other materials. This work applies advanced
101 materials analysis techniques to provide insight into the reaction pathways of Np denitration toward oxide
102 phases and novel microstructural evaluation of NpO₂ from this reaction pathway. Moreover, these
103 experimental and data analyses are unique because they were performed on materials from a production-
104 scale environment—rather than small, laboratory-scale experiments—and represent more realistic
105 samples for complicated processes.

106 2. Materials and Methods

107 *Caution: ²³⁷Np is an alpha-emitting radionuclide, and safe handling requires appropriate facilities and*
108 *qualified personnel.*

109 2.1 Experimental Work

110 Neptunium oxide samples were prepared according to the MDD production flowsheet. The operating
111 conditions for the MDD flowsheet for Np are fully described by Vedder,¹² but in short, they are as follows:
112 a ²³⁷Np stock with a 150–225 g/L concentration is modified with a 2.5:1 mole ratio of ammonium nitrate
113 and is fed at a rate of 3.5–5.5 mL/min into a rotary kiln. The kiln is at a 10° angle, purged with air, rotated
114 at approximately 10 rpm, and heated to a maximum of 675°C. The material from the kiln is then high-fired
115 to 1185°C to ensure that all product is NpO₂. Samples analyzed in this work were sub-sampled from
116 production runs in 2022.

117 Solid samples from the MDD kiln (referred to as *pre-fire*) and after high-firing (referred to as *post-fire*)
118 were analyzed by scanning electron microscopy coupled with energy-dispersive X-ray spectroscopy (SEM-
119 EDS) and by powder X-ray diffraction (pXRD). Samples from 4 production runs of ²³⁷Np target material
120 (07/26/2022, 08/31/2022, 10/19/2022, and 11/09/2022) were analyzed by both techniques. Samples for
121 SEM and pXRD analysis were taken from the same aliquot of material for consistency in analysis. For
122 pXRD, powder samples were analyzed in as-received condition on a Rigaku MiniFlex pXRD system
123 equipped with a Cu source using a scan range of 15–85° 2θ and a step size of 0.05° 2θ, with a silicon
124 standard analyzed monthly to control for phase-shift between samples. The Rigaku system is situated inside
125 a HEPA-filtered, negative-pressure glove box, allowing for sample preparation and analysis inside the glove
126 box. For SEM-EDS analysis, powder samples were prepared inside a HEPA-filtered, negative-pressure
127 glove box by sprinkling dry powders onto double-sided carbon tape affixed to an aluminum SEM stub.
128 Samples were not sputter coated. SEM analysis was performed on a Hitachi S4700 field-emission scanning
129 electron microscope at an accelerating voltage of 15 kV, current of 10 μA, and working distance of 12 mm.
130 An Oxford Xplore EDS detector (30 mm² silicon drift detector) equipped with AztecLiveLite microanalysis
131 software was coupled with SEM imaging for semi-quantitative determination of elemental composition in
132 samples.

133 2.2 Data Processing and Particle Size Analysis

134 Particle size analysis and distributions were performed using the Morphological Analysis for Material
135 Attribution (MAMA) software²⁴ for particle segmentation. This software is commonly used to quantify the
136 dimensions, distribution, and edge curvature of various particles both between samples and within a single
137 sample from scanning electron micrographs.^{22, 23} Following the methodology outlined by Olsen *et al.*²³, the
138 micrograph and particle segmentation flowsheet guided the micrograph selection process. Micrographs
139 were chosen to ensure that no single feature (particulate or void space) dominated the field of view and that
140 the particles were sufficiently large to discern from one another. This resulted in roughly 5,000×
141 magnification for the images, and a scale bar of 10 μm for half the image. In the MAMA software, the scale
142 bar was measured to be 510 pixels per 10 μm, resulting in a direct conversion of particle pixels to length.
143 Brightness and contrast of micrographs were altered to enhance particle edges so as to meet the
144 requirements of the micrograph selection flowsheet.²³ The inherent morphology of the sample oxides is
145 that they are aggregated. In order to avoid morphological alteration of the product, dispersion or breakage
146 of the aggregates was not performed in sample preparation. MAMA was selected as a workflow given that
147 literature²³ provides a firm metric for particle selection when oxide materials are clumped or in clustered
148 morphologies.

149 Within the MAMA interface, particles were segmented by employing a combination of the
150 software's internal automatic segmentation and manual segmentation where the watershed fitting method
151 failed to discern tonal differences between greys at particle edges. The flowsheet²³ was strictly adhered to,
152 to ensure analysis reproducibility among researchers and across research projects. It may appear that some
153 features that resemble particles are omitted; this is intentional. Particles needed to be distinct and not fused,
154 stacked, or covered to be included in analysis. Once particle segmentation was complete, the software
155 compiled characteristics for each particle and exported a batched spreadsheet. These data were analyzed
156 using Python's Plotly²⁵ figure generation package to produce box plots describing the median, quartile, and
157 outlier data. Plotly defines outliers as any values less than $4Q_1-3Q_3$ or greater than $4Q_3-3Q_1$. With this
158 formula for outlier determination, the outliers are selected quantitatively after particle segmentation and not
159 by the MAMA software itself, thereby removing inherent analytical bias and displaying outliers in the data
160 presentation instead of excluding them from statistical analysis altogether.

161 Of the many quantitative outputs from MAMA analysis, four were selected as representative
162 sample descriptors for this work. The outputs were chosen based on both the desired material properties for
163 NpO_2 targets and qualitatively observed properties of the materials from micrographs. Particle area
164 represents the direct measurement of the number of pixels in the segmented area of each particle and
165 converted to length using the 510 pixels to 10 μm conversion factor. Equivalent circular diameter (ECD)
166 represents the diameter of a perfect circle if the segmented area's pixels were rearranged into a circle instead
167 of the amorphous polygon. The ECD may be used as an estimate of grain size. Ellipse aspect ratio (EAR)
168 is the ratio of the major and minor axes within a particle (*i.e.*, is the particle long and narrow, or is it nearly
169 circular?). The particle circularity, on a scale of 0 to 1, represents how rounded and consistent a particle is
170 (*e.g.*, a square may be 0.05, an equilateral octagon may be 0.65, and a perfect circle is 1). In the reported
171 values, significant figures were reported with discretion. When values were calculated as a direct
172 conversion of pixels to micrometers, values were rounded so as not to report below a 1-pixel resolution
173 limit (as values reported below this would be akin to "Below Detection Limits" for traditional chemical
174 analyses). For calculated values using multiplication or ratios (Particle Area, ECD, and EAR), standard
175 significant figure rules were used after adhering to the 1-pixel resolution limit.

176

177

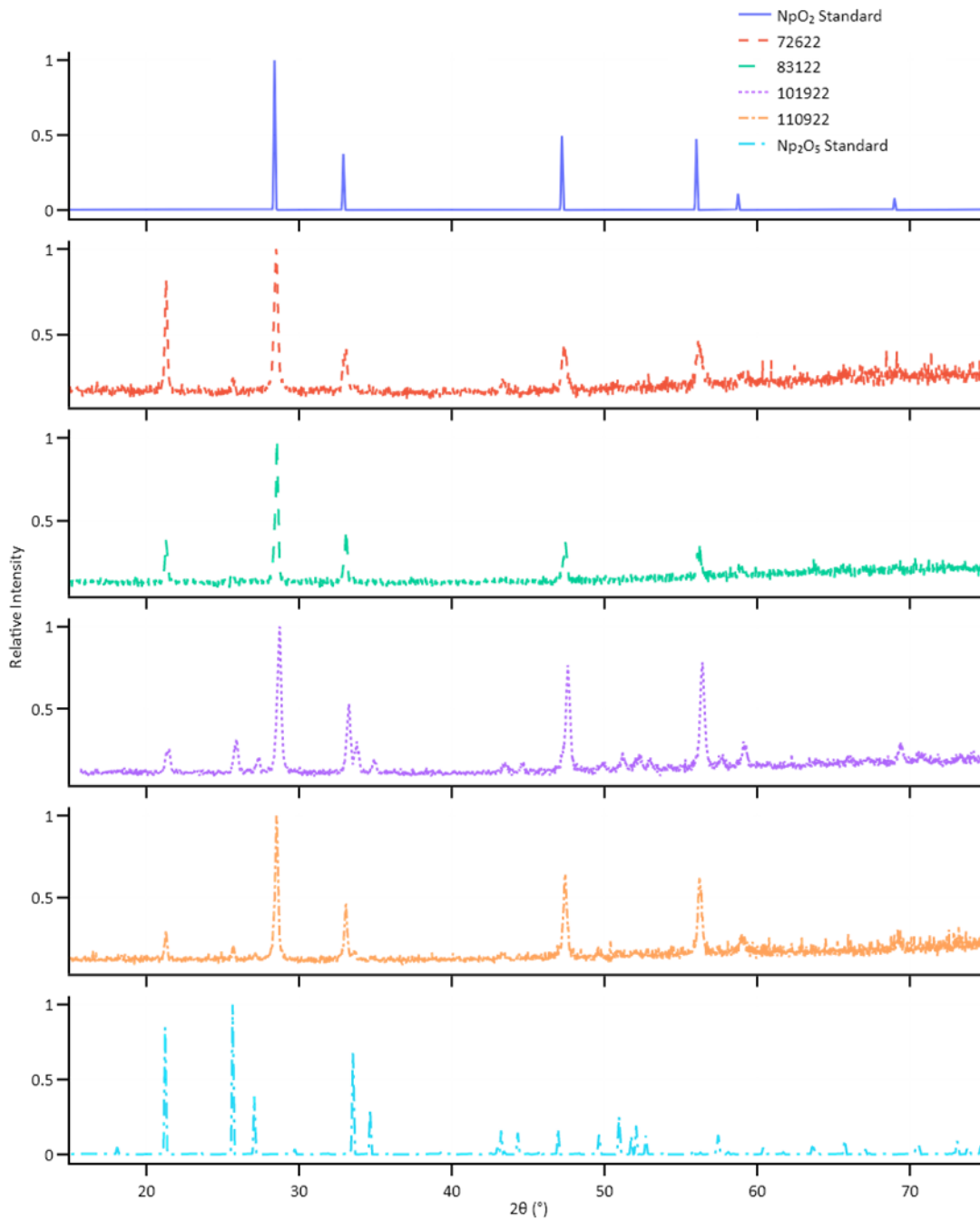
178

179

180 **3. Results**

181 **3.1 Modified Direct Denitration Product**

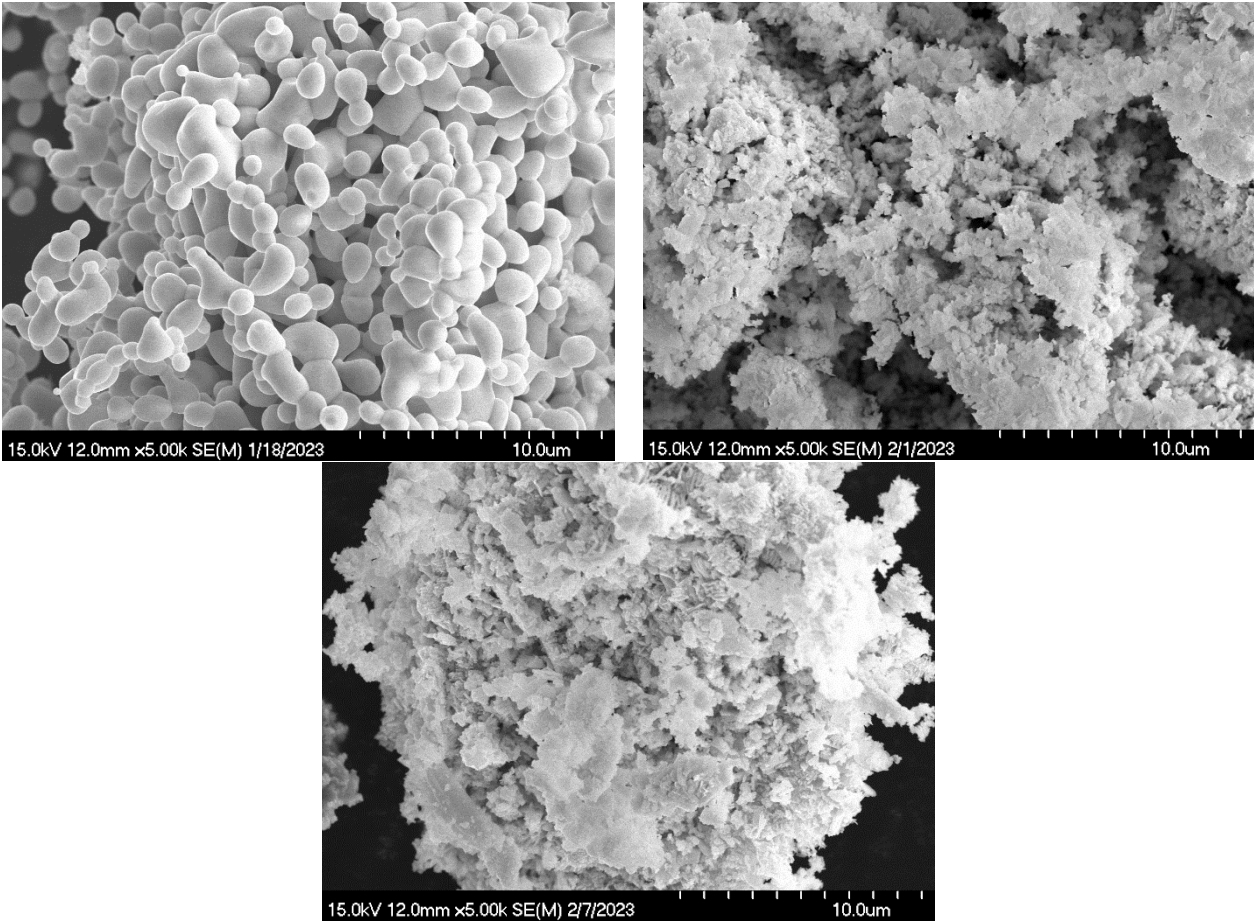
182 The product from the MDD kiln was analyzed from three separate kiln runs to determine the
183 morphology, particle size, bulk crystal phase, and trace element composition in the product. pXRD data
184 indicate that the product directly from the kiln (pre-fire) contains a mixture of both NpO_2 and Np_2O_5
185 (Figure 1). Complementary elemental analysis via EDS indicates that the powders contain primarily Np
186 and O at the surface of the material, with some traces of Al (SI Figures 2, 4, and 6). The presence of trace
187 Al in the sample may be due to residual Al metal powder inside gloveboxes used for the preparation of
188 samples.



189

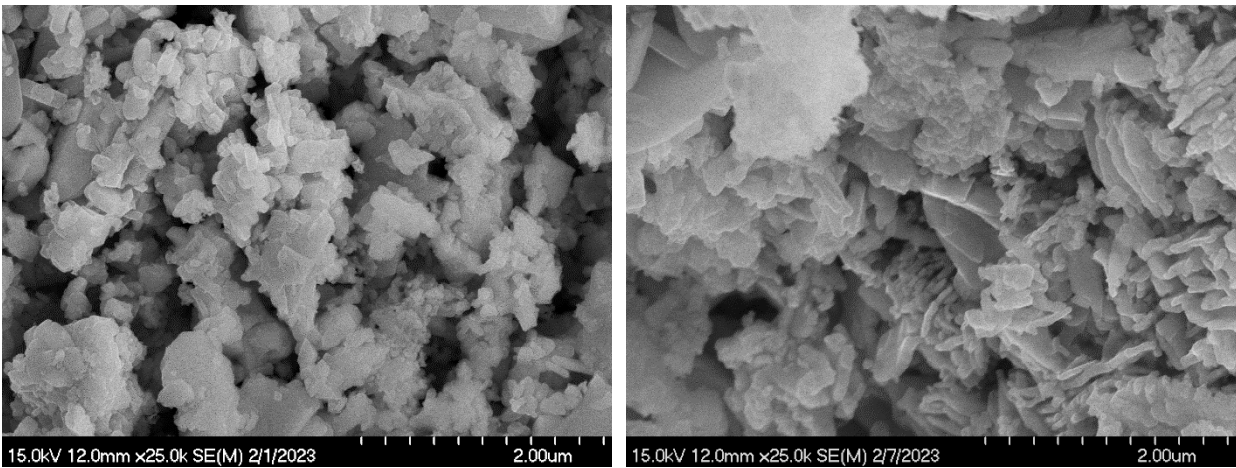
190 *Figure 1: Powder X-ray diffraction (pXRD) patterns of pre-fire product for each sampling event compared to the standard NpO_2*
 191 *(top²⁶) and Np_2O_5 (bottom²⁷) patterns.*

192 Powder samples from the MDD kiln contain a range of morphological features, as observed in
 193 scanning electron micrographs. All samples are complex aggregates but contain unique sub-particles.
 194 Some of the sub-particles observed are sub-rounded and granular in nature (Figure 2, top left), whereas
 195 other samples contain less distinct, clumped particles (Figure 2, top right and bottom).



196 *Figure 2: Scanning electron micrographs of product from the MDD kiln (pre-fire material) from 08/31/2022 (top left),*
 197 *10/19/2022 (top right) and 11/09/2022 (bottom) at 5,000× magnification.*

198 Higher magnification micrographs elucidate the shape and form of the clumped sub-particles, showing
 199 that one sample contains tabular particles (Figure 3, left) and another contains both tabular and platy
 200 particles, some of which have a layered spatial grouping (Figure 3, right).

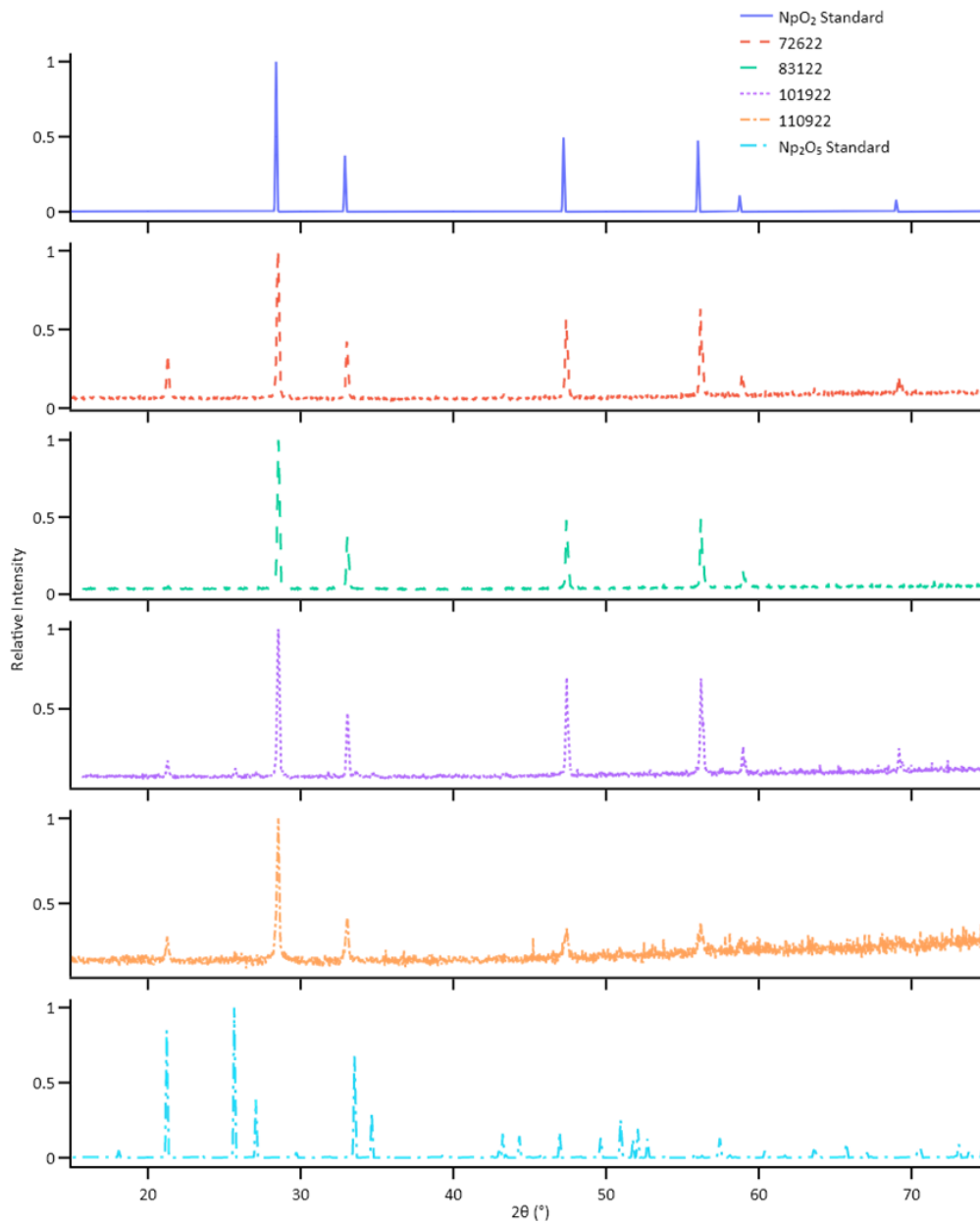


201 *Figure 3: Scanning electron micrographs of product from the MDD kiln (pre-fire material) from 10/19/2022 (left) and*
 202 *11/09/2022 (right) at 25,000× magnification.*

203

204 3.2 High-fired Product

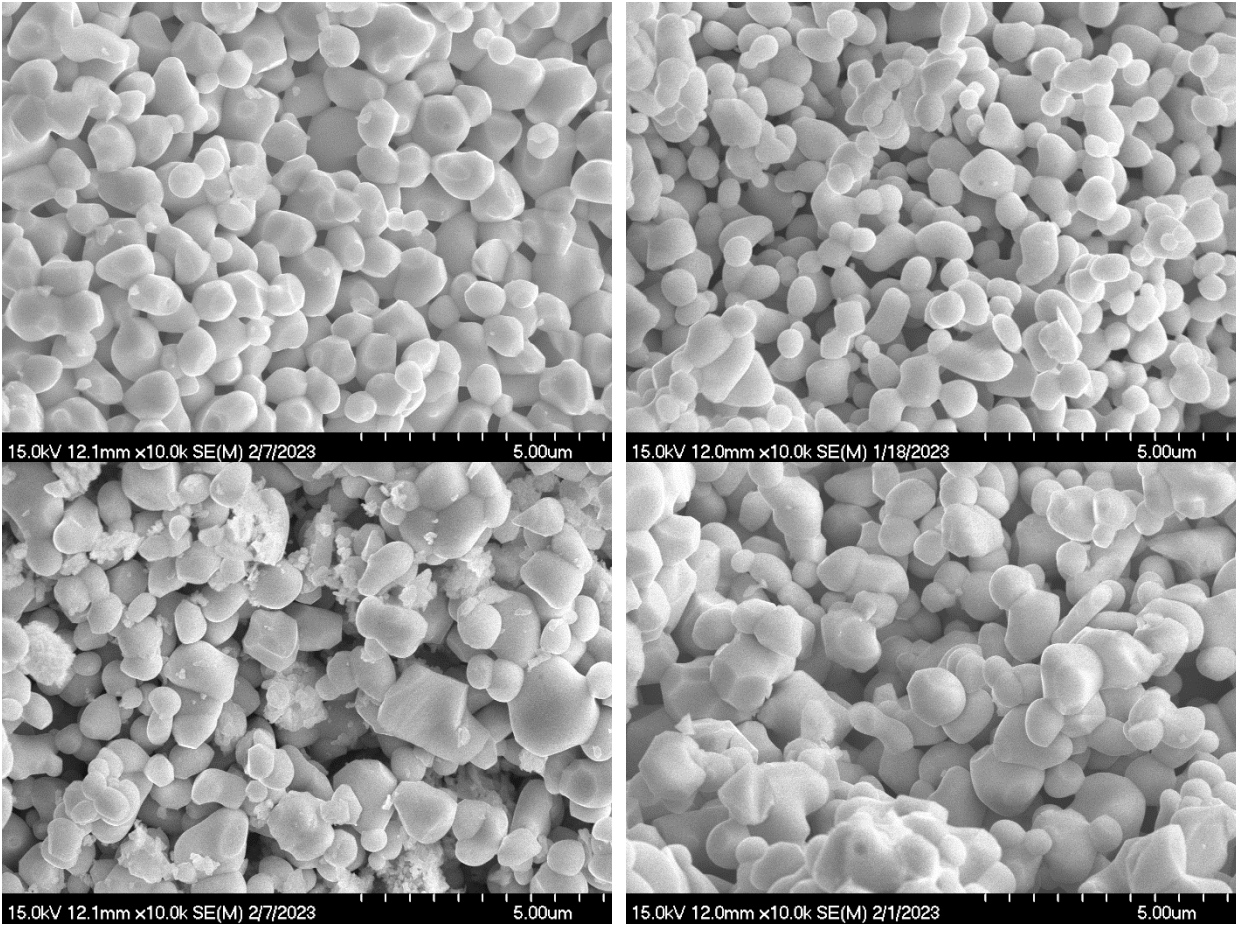
205 After high-firing to 1185°C, the final product was also analyzed to determine the morphology,
206 particle size, bulk crystal phase, and trace element composition in the same manner as the pre-fire
207 product. pXRD data show that the high-fired product contains primarily NpO_2 (Figure 4). However, some
208 peaks corresponding to Np_2O_5 were found in some of the samples, but not consistently. Preferential
209 orientation of Np_2O_5 particles within the sample may modify Bragg line intensities and make them
210 strongly different from those expected for an "ideal powder" (i.e. with random orientation crystallites).
211 Multiple potential sources of Np_2O_5 in the high-fired material are still under investigation. Elemental
212 analysis of the samples via EDS shows similar results to those of the pre-fire samples: powders composed
213 primarily Np and O at the surface of the material, with some traces of Al (SI Figures 1, 3, 5, and 7).



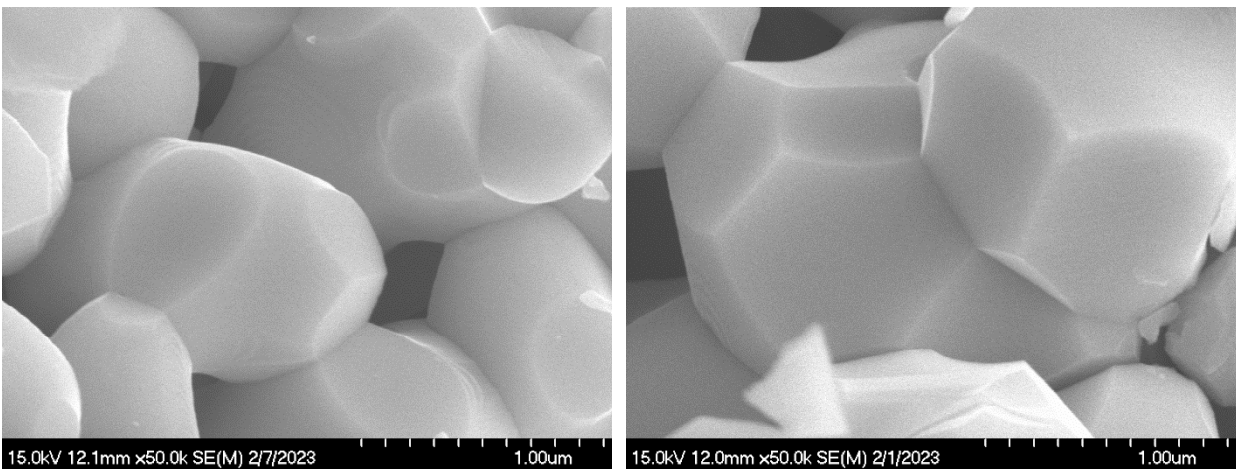
214

215 *Figure 4: pXRD patterns of high-fired product for each sampling event, compared to the standard NpO_2 (top²⁶) and Np_2O_5*
 216 *(bottom²⁷) patterns.*

217 Micrographs of the high-fired powders show notable consistency among the four sets of samples
 218 analyzed. The high-fired powders are polycrystalline, complex aggregates. The sub-particles within the
 219 aggregates are a mixture of sub-rounded grains, faceted crystalline particles, and fines (Figure 5). The
 220 faceted crystalline particles have smooth surfaces (Figure 6).



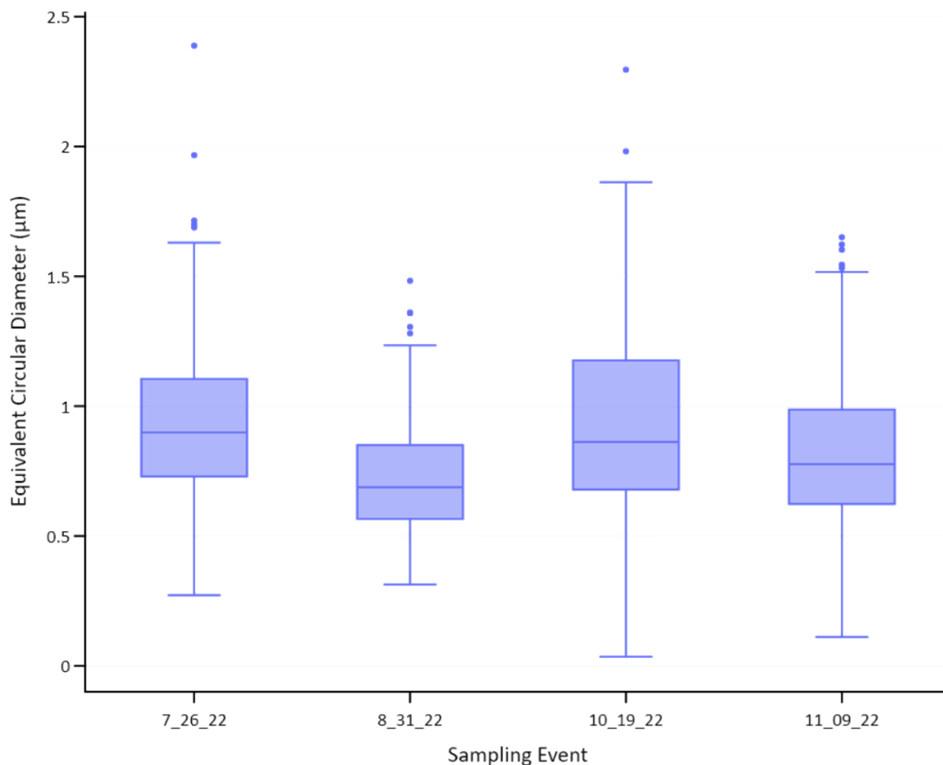
221 *Figure 5: Scanning electron micrographs of high-fired product (clockwise from top left) from 07/26/2022, 08/31/2022,*
 222 *10/19/2022 and 11/09/2022 at 10,000× magnification.*



223 *Figure 6: Scanning electron micrographs of high-fired product from 07/26/2022 (left) and 10/19/2022 (right) showing faceted*
 224 *grains at 50,000× magnification.*

225 Analysis of particles from high-fired samples in MAMA provides quantitative statistical
 226 comparisons of qualitatively similar high-fired products. The initial qualitative homogeneity observed in
 227 the high-fired samples (Figure 5) is confirmed by the quantitative data: the mean ECD values all fall
 228 within one standard deviation (Figure 7, Table 1), and the remaining box plots present similar
 229 confirmations of the homogeneity (SI Figures 8–10). Mean ECD values ranged from 0.7 to 0.9 μm (Table

230 1). Additionally, the calculated values for circularity and EAR were nearly invariant between samples
231 (Table 1), further supporting quantitative homogeneity of the products between runs. Additional box plots
232 for values in Table 1 are presented in the supporting information (SI Figures 8–10). Examples of particle
233 segmentation for each micrograph can also be found in the supporting information (SI
234 Figures 11–14).



235
236 *Figure 7: Equivalent circular diameter (ECD) box plot distribution of particles in each high-fired sampling event. The ECD*
237 *represents the diameter of each particle if the particle's total pixel area was rearranged into a perfect circle.*

238
239
240
241
242
243
244
245

246 *Table 1: Particle area, ECD, ellipse aspect ratio, and circularity distribution statistics for each high-fired sampling date based*
 247 *on MAMA segmenting and analysis.*

Run Date	Sample Size	Characteristic	Mean	Standard Deviation	Max	Min
7/26/22	202	Particle Area (μm^2)	0.77	0.56	4.48	0.06
		Equivalent Circular Diameter (μm)	0.9	0.3	2.4	0.3
		Ellipse Aspect Ratio	1.33	0.23	2.50	1.02
		Circularity	0.72	0.08	0.89	0.37
8/31/22	245	Particle Area (μm^2)	0.45	0.28	1.73	0.08
		Equivalent Circular Diameter (μm)	0.7	0.2	1.5	0.3
		Ellipse Aspect Ratio	1.33	0.27	2.36	1.02
		Circularity	0.75	0.07	0.90	0.45
10/19/22	116	Particle Area (μm^2)	0.82	0.69	4.14	0.00
		Equivalent Circular Diameter (μm)	0.9	0.4	2.3	0.0(3)
		Ellipse Aspect Ratio	1.36	0.34	3.73	1.03
		Circularity	0.74	0.10	0.88	0.00
11/09/22	230	Particle Area (μm^2)	0.57	0.41	2.14	0.01
		Equivalent Circular Diameter (μm)	0.8	0.3	1.7	0.1
		Ellipse Aspect Ratio	1.32	0.26	2.46	1.02
		Circularity	0.75	0.08	0.91	0.50

248

249

250 4. Discussion

251 The combination of solid phase characterization techniques and post-characterization data
 252 analysis illuminates the fundamentals of MDD as a synthesis route for NpO_2 . The data suggest that the
 253 MDD process produces a material that is a mixture of NpO_2 and Np_2O_5 , which has a variable and often
 254 mixed morphology. The cause of variability in the product from the MDD process is still under
 255 investigation due to the small data set, and continued monitoring of the production line is warranted to
 256 elucidate trends. However, it appears that the high-firing process eliminates much of the variability in the
 257 material, forming a primarily NpO_2 product with consistent grain sizes and morphology. This
 258 homogeneity is supported by quantitative particle analysis, which shows consistent particle areas,
 259 diameters, and circularity among sample sets. The lack of statistically significant differences between
 260 particle diameters and the other shape characteristics reinforces the impact of the high-firing process on
 261 reducing product heterogeneity. The qualitative and quantitative observations of homogeneity in the high-
 262 fired MDD product suggest that heating samples to 1185°C ensures that morphological imperfections are
 263 eliminated in the process of conversion to NpO_2 . At such high temperatures, the oxide can recrystallize,
 264 thereby reducing surface defects, surface energy, and surface area of the material and leading to the most
 265 thermodynamically stable state of the material. The morphology of the high-fired product, a
 266 polycrystalline aggregate, presents remarkable similarity to other published microstructures of high-fired
 267 NpO_2 . For example, NpO_2 synthesized via oxalate precipitation and calcination was reported to have

268 average grain diameters in a polycrystalline aggregate ranging from 11 to 371 nm at calcination
269 temperatures in the 400–900°C range, respectively.²⁸

270 The analysis of Np phases from MDD can also help elucidate the reaction pathway for denitration
271 of Np nitrates to oxides. The reaction pathways for U denitration are well documented, as outlined in the
272 introduction, but remain unreported for Np. Although the data collected in this work do not provide a
273 direct measure of the reaction pathway, they do provide suggestions about the route. Specifically, the
274 pXRD data indicate that there is an Np₂O₅ intermediate in the reaction, which is not analogous to the U
275 system. In Equations 1–3, the uranium double salt decomposes step-wise to produce UO₃. Given the
276 differences in oxidation state between Np and U, this result is not unexpected. However, the findings
277 present additional questions regarding the reaction mechanism of Np ammonium nitrate decomposition.
278 The presence of Np₂O₅ suggests that the Np does not undergo oxidation–reduction reactions during the
279 initial decomposition stages of the ammonium nitrate salt: rather, it reduces to Np(IV) after full
280 conversion to Np₂O₅ and at higher temperatures. Particularly, the data suggest that conversion to NpO₂
281 takes place during the high-firing process. However, the presence of both NpO₂ and Np₂O₅ in samples
282 from the MDD kiln raises questions about the temperatures at which various steps of decomposition and
283 conversion occur, which cannot be isolated from the production samples.

284 5. Conclusions

285 MDD reactions are used to convert feedstock of Np ammonium nitrate to NpO₂ for ²³⁷Np targets
286 for ²³⁸Pu production. The approach to NpO₂ production through MDD was pioneered at ORNL for U and
287 MOX phases, but it requires continual study, especially on the unique chemistry of Np, for both economic
288 and engineering optimization of production flowsheets. Robust and reliable production of ²³⁷NpO₂ is
289 critical for the ongoing supply needs of ²³⁸Pu for RTGs associated with NASA missions. Analysis of the
290 material from the MDD kiln indicates that the kiln produces a mixture of NpO₂ and Np₂O₅ with a variety
291 of morphologies. The product, composed of complex aggregates, showed mixtures of clumped, tabular,
292 and platy particles. The high-firing of the kiln product produced NpO₂ with some evidence of Np₂O₅
293 peaks, while qualitative and quantitative observations confirmed morphological homogeneity.
294 Quantitative NpO₂ analysis indicated low standard deviations in particle diameter between runs and
295 consistent circularity, areas, and particle elongation. Np materials analysis using the MAMA software has
296 not been previously reported.

297 Future efforts on characterization of ²³⁷Np target materials will focus on continued measurement
298 of materials from ongoing production to increase data set sizes and elucidate trends over years of
299 production runs. Analysis of production-scale materials presents a challenge because of the effects of
300 chemical process scaling, including the large number of variables in the system and the potential for
301 heterogenous chemical environments within the same system. Targeted laboratory-scale experiments can
302 assist in deconvolution of production data, including such key efforts as determination of the Np
303 ammonium nitrate decomposition pathway. Thorough understanding of the chemical phenomena
304 underlying this production process provides not only advantages for production optimization, but also for
305 advancement of the chemistry of transuranic materials, which present unique challenges for handling and
306 characterization.

307

308

309

310 **6. Acknowledgments**

311 This work is supported by the ²³⁸Pu Supply Program at the US Department of Energy's Oak Ridge
312 National Laboratory with funding provided by the Science Mission Directorate of the National Aeronautics
313 and Space Administration and administered by the US Department of Energy, Office of Nuclear Energy,
314 under contract DEAC05-00OR2272.

315 The authors acknowledge the contributions and assistance of Phil Burke, Cory Dryman, John Dyer,
316 Kaara Patton, Curt Porter, and Joseph Renfro in chemical process operations and powder sample
317 preparation efforts.

318

319 **7. References**

320

- 321 1. NRC, *Radioisotope Power Systems*. 2009.
- 322 2. Burney, G.; Harbour, R., *Radiochemistry of neptunium*. National Academies: 1974.
- 323 3. Myrick, R.; Folger, R., Fabrication of Targets for Neutron Irradiation of Neptunium Dioxide.
324 *Industrial & Engineering Chemistry Process Design and Development* **1964**, 3 (4), 309-313.
- 325 4. Collins, E. D.; Morris, R. N.; McDuffee, J. L.; Mulligan, P. L.; Delashmitt, J. S.; Sherman, S. R.;
326 Vedder, R. J.; Wham, R. M., Plutonium-238 Production Program Results, Implications, and
327 Projections from Irradiation and Examination of Initial NpO₂ Test Targets for Improved Production.
328 *Nuclear Technology* **2022**, 1-8.
- 329 5. Depaoli, D. W.; Benker, D.; Delmau, L. H.; Sherman, S. R.; Riley Jr, F.; Bailey, P. D.; Collins,
330 E. D.; Wham, R. M. *Process Development for Plutonium-238 Production at Oak Ridge National*
331 *Laboratory*; Oak Ridge National Lab.(ORNL), Oak Ridge, TN (United States): 2019.
- 332 6. Wham, R.; DePaoli, D.; Collins, E. D.; Delmau, L. H.; Benker, D. *PROCESS CHEMISTRY FOR*
333 *THE PRODUCTION OF PLUTONIUM-238*; Oak Ridge National Lab.(ORNL), Oak Ridge, TN
334 (United States): 2019.
- 335 7. Collins, E. D., Advanced thermal denitration conversion processes for aqueous-based reprocessing
336 and recycling of spent nuclear fuels. In *Reprocessing and Recycling of Spent Nuclear Fuel*, 2015; pp
337 313-323.
- 338 8. Mailen, J.; Pruett, D.; McTAGGART, D. *Direct thermal denitration to prepare mixed oxides for*
339 *nuclear fuel fabrication*; Oak Ridge National Lab.(ORNL), Oak Ridge, TN (United States): 1982.
- 340 9. Haas, P. A.; Arthur, R. D.; Stines, W., Development of Thermal Denitration to Prepare Uranium
341 Oxide and Mixed Oxides for Nuclear Fuel Fabrication. **1981**.
- 342 10. Notz, K. J.; Haas, P. A., Properties and thermal decomposition of the double salts of uranyl nitrate-
343 ammonium nitrate. *Thermochimica acta* **1989**, 155, 283-295.
- 344 11. Kim, B. H.; Lee, Y. B.; Prelas, M. A.; Ghosh, T. K., Thermal and X-ray diffraction analysis studies
345 during the decomposition of ammonium uranyl nitrate. *J Radioanal Nucl Chem* **2012**, 292 (3), 1075-
346 1083.
- 347 12. Vedder, R. J. *Oak Ridge National Laboratory Preparation of Sintered 237NpO₂ Pellets for*
348 *Irradiation to Produce 238Pu Oxide*; ORNL/TM-2017/728; Oak Ridge National Laboratory: 2018.
- 349 13. Wham, R. M.; Owens, R. S.; Vedder, R. J.; Miller, J. H.; Pierce, S. In *AUTOMATION OF*
350 *NEPTUNIUM OXIDE-ALUMINUM TARGET FABRICATION*, ANS NETS 2019 – Nuclear and
351 Emerging Technologies for Space, Richland, WA, American Nuclear Society: Richland, WA, 2019.
- 352 14. Choppin, G. R., Solution Chemistry of the Actinides. *Radiochimica Acta* **1983**, 32 (1-3), 43-54.
- 353 15. Duffey, J. *Lab Scale Production of NpO₂*; SRS (US). Funding organisation: US Department of
354 Energy (United States): 2003.
- 355 16. Duffey, J. *Characterization of Neptunium Oxide Generated Using the HB-Line Phase II Flowsheet*;
356 SRS: 2003.
- 357 17. Porter, J., Production of Neptunium Dioxide. *Industrial & Engineering Chemistry Process Design*
358 *and Development* **1964**, 3 (4), 289-292.

- 359 18. Severynse, T. *Nuclear Material Processing at the Savannah River Site*; Westinghouse Savannah
360 River Company, Aiken, SC (United States); Westinghouse Savannah River Co., Aiken, SC (United
361 States): 1998.
- 362 19. Peruski, K. M.; Koehler, K. C.; Powell, B. A., Grain boundary facilitated dissolution of
363 nanocrystalline NpO₂ (s) from legacy waste processing. *Environmental Science: Nano* **2020**, 7 (8),
364 2293-2301.
- 365 20. Karelin, A.; Krot, N.; Kozlova, R.; Lobas, O.; Matukha, V., Thermal decomposition of Np (IV)
366 and Pu (III, IV) oxalates. *Journal of Radioanalytical and Nuclear Chemistry* **1990**, 143 (1), 241-252.
- 367 21. Lindsay, J. W.; Robinson, H. N.; Bramlet, H. L.; Johnson, A. J., The thermal decomposition of
368 neptunium (IV) oxalate. *Journal of Inorganic and Nuclear Chemistry* **1970**, 32 (5), 1559-1567.
- 369 22. Schwerdt, I. J.; Olsen, A.; Lusk, R.; Heffernan, S.; Klosterman, M.; Collins, B.; Martinson, S.;
370 Kirkham, T.; McDonald, L. W., Nuclear forensics investigation of morphological signatures in the
371 thermal decomposition of uranyl peroxide. *Talanta* **2018**, 176, 284-292.
- 372 23. Olsen, A. M.; Richards, B.; Schwerdt, I.; Heffernan, S.; Lusk, R.; Smith, B.; Jurrus, E.;
373 Ruggiero, C.; McDonald, L. W. I. V., Quantifying Morphological Features of α -U₃O₈ with Image
374 Analysis for Nuclear Forensics. *Analytical Chemistry* **2017**, 89 (5), 3177-3183.
- 375 24. Gaschen, B. K.; Bloch, J. J.; Porter, R.; Ruggiero, C. E.; Oyen, D. A.; Schaffer, K. M. *MAMA*
376 *User Guide v2.0.1*; United States: United States, 2016.
- 377 25. Collaborative data science. Plotly Technologies Incorporated, : Montreal, QC, 2015.
- 378 26. Zachariasen, W. H., Crystal chemical studies of the 5f-series of elements. XII. New compounds
379 representing known structure types. *Acta Crystallographica* **1949**, 2, 388-390.
- 380 27. Forbes, T. Z.; Burns, P. C.; Skanthakumar, S.; Soderholm, L., Synthesis, Structure, and Magnetism
381 of Np₂O₅. *Journal of the American Chemical Society* **2007**, 129 (10), 2760-2761.
- 382 28. Peruski, K. M.; Powell, B. A., Effect of calcination temperature on neptunium dioxide
383 microstructure and dissolution. *Environmental Science: Nano* **2020**.